

Point-mass sensitivity of gravimetric satellites

Robert Spero

robert.spero@jpl.nasa.gov
Jet Propulsion Laboratory, Pasadena, CA 91109

Received 12 December 2020;

Abstract

Frequency-domain expressions are found for gradiometer and satellite-to-satellite tracking measurements of a point source on the surface of the Earth. The maximum signal-to-noise ratio as a function of noise in the measurement apparatus is computed, and from that the minimum detectable point mass is inferred. A point mass of magnitude $M_3 = 100$ Gt gives a signal-to-noise ratio of 3 when a GOCE-like gradiometer passes directly over the mass. On the satellite-to-satellite tracking mission GRACE-FO $M_3 = 1.3$ Gt for the microwave instrument and $M_3 = 0.5$ Gt for the laser ranging interferometer. The sensitivity of future GRACE-like missions with different orbital parameters and improved accelerometer sensitivity is explored, and the optimum spacecraft separation for detecting point-like sources is found. The future-mission benefit of improving the accelerometer sensitivity for measurement of non-gravitational disturbances is shown by the resulting reduction of M_3 , to as small as 7 Mt for 500 km orbital altitude and optimized satellite separation of 900 km.

© 2020 COSPAR. Published by Elsevier Ltd All rights reserved.

1. Introduction

A global gravity map is the principal data product of satellite gravity missions. Previously CHAMP (Reigber et al. (2003)), GRACE (Tapley et al. (2004)), and GOCE (Drinkwater et al. (2006)) collected data to map the Earth's gravity, and GRAIL (Konopliv et al. (2013)) measured the Moon's gravity. Currently GRACE Follow-On (GRACE-FO, Landerer et al. (2020)) is extending the GRACE data record, with increased ranging precision afforded by its laser ranging interferometer (LRI, Abich et al. (2019)).

As pointed out by Watkins et al. (2015), the most commonly used method of analyzing satellite gravity data is based on global gravity fields expressed in terms of spherical harmonic basis functions. An alternative to spherical harmonics is the mass concentration, or mascon, model. Starting with Wong et al. (1971), the mascon approach was applied to single-satellite lunar orbital measurements to infer the surface gravity of the moon. Mascons can be modeled as many discrete sources (Pollack (1973), Watkins et al. (2005)) that cover the globe, or used to solve for regional fields. Han (2013) applied mascons

to GRAIL data to solve for regional fields of the Moon.

Though they differ slightly in assumptions and results, the spherical harmonic and mascon methods are constructed to answer the same question: what is the gravity field that is most consistent with measurements? Here we address a different question: what is the limit to measurement precision of a point-like mass on the surface? This is an artificial model, a single mascon, that is not directly applicable to the geodetic agenda of measuring the Earth's gravity. We do not attempt to replicate the global gravity-field inversion achieved by the usual many-mascon analysis. Rather, the motivation for this analysis is twofold: to provide a single-number figure of merit, namely the minimum detectable isolated point mass perturbation, and to find the optimal filter for such a detection. The minimum detectable mass M_3 is defined as the point mass that gives a signal-to-noise ratio $\rho = 3$ in a single orbital pass directly over the point mass. It is calculated by applying the Wiener optimal filter to the problem of detecting a signal of known waveform, against a background specified by instrument noise power spectral density (Wainstein and Zubakov (1970)). A comparison of

M_3 for different orbital configurations and instrument sensitivities guides the design of future missions. Additionally, we find the optimum satellite separation in GRACE-like missions for a specified instrument noise power spectral density.

2. Gradiometer Mass Sensitivity

Consider a gradiometer flying directly over a point mass M at altitude h , Figure 1 left. At orbital altitude $h = 330$ km, the

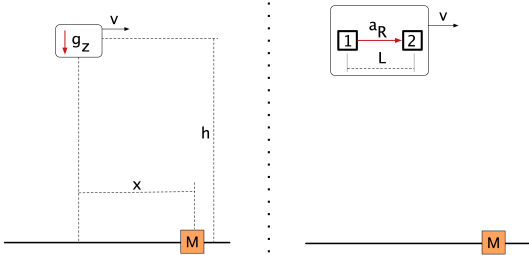


Fig. 1. Measurement of gravitational field from a point mass M at along-track distance x , altitude h , and velocity v . *Left:* Vertical gradient g_z . *Right:* Differential acceleration a_R between spacecraft 1 and 2 with average separation L .

along-track velocity v is the orbital velocity $v_o = 7.7$ km/s and the along-track distance x changes at approximately constant rate, $x = v_o t$. The acceleration at the spacecraft in the vertical, z direction is $a_z = -GMz/(x^2 + z^2)^{3/2}$, and the gradient in the z direction is $g_z = da_z/dz = GM[3z^2(x^2 + z^2)^{-5/2} - (x^2 + z^2)^{-3/2}]$. G = Newton's constant of gravitation. Substituting $z \rightarrow h$ and $x \rightarrow v_o t$,

$$g_z(t) = \kappa_g M \left[3(1 + [f_h t]^2)^{-5/2} - (1 + [f_h t]^2)^{-3/2} \right] \quad (1)$$

where $\kappa_g M = GM/h^3 = 1.85 \times 10^{-3}$ mE with $M = 1$ Gt and $f_h = v_o/h = 23$ mHz; 1 mE = 1×10^{-12} s $^{-2}$. At $t = 0$, when the gradiometer is directly above the source mass, the gradient reaches its maximum value $g_z = 2\kappa_g M$. At $x = \pm\sqrt{2}h$, $g_z = 0$.

The Fourier transform of $p(t)$ is defined by $\mathcal{F}[p(t)] \equiv p(f) = \int_{-\infty}^{\infty} dt p(t) \exp(-2\pi i f t)$. Applying the Fourier transform to $g_z(t)$:

$$g_z(f) = \kappa_g M \frac{4\pi f}{f_h^2} \left[K_1 \left(\frac{2\pi f}{f_h} \right) + \frac{2\pi f}{f_h} K_0 \left(\frac{2\pi f}{f_h} \right) \right] \quad (2)$$

where K_n is the modified Bessel function of the second kind, order n . From Abramowitz and Stegun (1964), Section 9.7.2, $K_n(z) \sim \sqrt{\pi/(2z)} e^{-z}$, where \sim indicates approximately equal for large z . At frequency $f \gg f_h$, the measurement response is attenuated approximately exponentially with e -folding frequency $f_h/(2\pi) = 3.7$ mHz. This corresponds to harmonic order $N = f_h/(2\pi f_1) = 20$, where $f_1 = 0.183$ mHz is the orbital frequency.

The signal-to-noise ratio ρ depends on the signal and the power spectral density of the gradiometer noise, $S_g(f)$. Define the frequency-dependent signal-to-noise-ratio density SNRD as

$$W_{g_z}(f) = \frac{|g_z(f)|^2}{S_g(f)}. \quad (3)$$

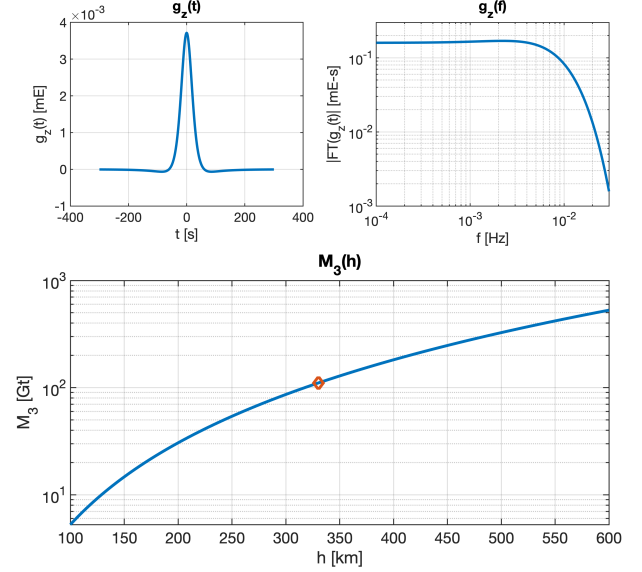


Fig. 2. Orbiting gradiometer vertical gradient response to a point mass. *Upper-left:* $g_z(t)$, z -direction gradient in time domain, Equation 1; *Upper-right:* $g_z(f)$ = Fourier transform, Equation 2; *Lower:* M_3 = Detectable mass with signal-to-noise = 3, Equation 5.

In general, ρ depends on what filtering is applied to the instrument output. After Flanagan and Hughes (1998), with optimum filtering the maximum signal-to-noise ratio per unit source mass ρ' is

$$\rho' = \sqrt{4 \int_0^{\infty} W'_{g_z}(f) df}. \quad (4)$$

Prime superscripts indicate quantities normalized by the source mass: $\rho' = \rho/M$ and $W'_{g_z}(f) = W_{g_z}(f)/M^2$. It follows that the minimum detectable point mass with $\rho = 3$ is

$$M_3 = \frac{3}{\sqrt{4 \int_0^{\infty} W'_{g_z}(f) df}}. \quad (5)$$

The lower panel of Figure 2 shows M_3 as a function of orbital altitude h for a gradiometer limited by white spectral noise $S_g(f) = 1$ mE/ $\sqrt{\text{Hz}}$ (approximated value for GOCE from Touboul et al. (1999), Touboul et al. (1999a)). At $h = 330$ km, $M_3 = 100$ Gt and the minimum observable gradient at the peak time $t = 0$ is $2\kappa_g M = 0.37$ mE.

3. Sensitivity of GRACE-like measurements

The measurement configuration and signal parameters for the low-low satellite-to-satellite tracking (SST) of GRACE and GRACE-FO are shown in Figure 1, right. The primary signal is the along-track differential position of the spacecraft, measured by microwave ranging or laser interferometry.

3.1. Single Spacecraft Acceleration

For simplicity, the Flat-Earth approximation (Tapley (1997)) is used. This approximation neglects centrifugal acceleration,

which introduces an error of less than 20% at Fourier frequencies greater than 2 mHz (Ghobadi-Far et al. (2018), Figure 1; Müller (2017), Figure 1.7). In this approximation, the acceleration on spacecraft 1 flying over point mass M at along-track distance x is $a_1 = -GMx/(h^2 + x^2)^{3/2}$.

Define the acceleration per unit source mass, $a'_1 = a_1/M$. Then

$$a'_1 = -\frac{Gv_o}{(h^2 + v_o^2 t^2)^{3/2}} \quad (6)$$

Converting to frequency space,

$$a'_1(f) = \mathcal{F}[a'_1(t)] = \frac{4\pi i f G K_0 \left(\frac{2\pi f}{f_h}\right)}{v_o^2}. \quad (7)$$

3.2. Range Acceleration Signal

The acceleration experienced by spacecraft 2 is the same as spacecraft 1 at distance L , but delayed by $\tau = L/v_o$. The resulting (along-track) range acceleration between the spacecraft (Figure 3, left) is similar to what Han (2013) computed for the response of the GRAIL spacecraft to regional lunar gravity. The peak range acceleration a_R^p is

$$a_R^p = \frac{GL}{(h^2 + (L/2)^2)^{3/2}} M \equiv \kappa_R M, \quad (8)$$

where $\kappa_R = GL(h^2 + (L/2)^2)^{-3/2}$.

Using the identity $\mathcal{F}(\text{delay } \tau) = \exp(-2\pi i f \tau)$, the range acceleration in the frequency domain, $a_R(f)$, is given by

$$a'_R(f) = a'_1(f)(1 - e^{-2\pi i f \tau}) \quad (9)$$

$$|a'_R(f)| = 2|a'_1(f)| \sin(\pi f \tau) \quad (10)$$

That is, in the frequency domain the range acceleration is the single-satellite acceleration multiplied by $2|\sin(\pi f \tau)|$. For $f \ll 1/\tau$, $|a_R(f)| \propto L$, which is the response for the spacecraft pair acting as a gradiometer. The response departs from that of a gradiometer at large L , most conspicuously in the form of high-frequency nulls where the signal vanishes. The first null is at $f_{\text{null}} = 1/\tau = 38$ mHz for low-Earth orbit and $L = 200$ km, as recognized by Wolff (1969). In degree-variance evaluations of measurement sensitivity, the first null is expressed as a maximum in geoid height error at degree $N = f_{\text{null}}/f_1 = 216$ for $L = 200$ km, and $N = 86$ for $L = 500$ km, where $f_1 =$ orbital frequency = 0.176 mHz.

From Equations 7 and 10,

$$|a'_R(f)| = \frac{8\pi f G}{v_o^2} \left| K_0 \left(\frac{2\pi f}{f_h} \right) \right| \left| \sin \left(\frac{2\pi f}{f_L} \right) \right|, \quad (11)$$

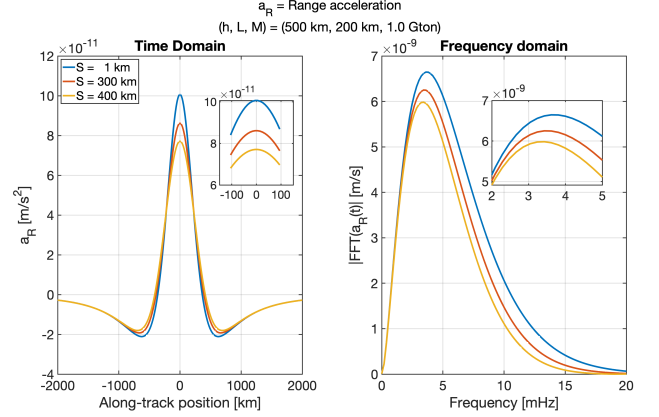


Fig. 3. Range acceleration resulting from a square mass centered under the flight along-track path. Orbital altitude h , average spacecraft separation L and source mass M are indicated in the title. The separate traces are for squares of side S indicated in the legend. *Left*: time domain, $a_R(t)$; *Right*: Fourier Transform, $a_R(f)$.

where

$$\begin{aligned} v_o &= \text{orbital velocity} && = 7.6 \text{ km/s} \\ h &= \text{orbital altitude} && = 500 \text{ km} \\ L &= \text{spacecraft separation} && = 200 \text{ km} \\ f_h &= \frac{v_o}{h} && = 15.2 \text{ mHz} \\ f_L &= \frac{v_o}{L/2} && = 76 \text{ mHz} \\ \tau &= \frac{L}{v_o} && = 26 \text{ s} \\ \kappa_R &= \frac{GL}{(h^2 + (L/2)^2)^{3/2}} && = 0.101 \text{ nm/s}^2/\text{Gt}. \end{aligned}$$

These numerical values apply to GRAIL-FO. The approximately exponential attenuation with frequency of $|a_R(f)|$ has e -folding frequency 2.5 mHz, corresponding to harmonic order $N = 14$.

To explore the valid realm of the point-mass approximation, Figure 3 shows the range acceleration signal from a square-shaped planar mass of side length S , computed by numerical integration. The $S=1$ km result is in agreement with the point-mass analytical calculation, which is valid at the 20% level for sources as large as $S=300$ km. Henceforth, we restrict our analysis to the signal from a point source.

Equation 11 gives the measurement impulse response; that is, the range acceleration frequency response to a point mass input. This facilitates the direct comparison of signal and noise amplitudes as computed in the following section, and yields an expression for the minimum detectable mass for GRACE-like measurements of point source perturbations to surface gravity.

3.3. Noise and Mass Sensitivity

Consider the range measurement made by the laser ranging interferometer (LRI) on GRAIL-FO. Assuming the measurement resolution is limited by the thermal noise of the laser reference cavity (Numata et al. (2004)), the displacement noise

root power spectral density (rpsd) \tilde{x}_{LRI} and strain rpsd \tilde{x}_{LRI}/L are given by

$$\tilde{x}_{\text{LRI}}(f)/L = x_c/\sqrt{f}, \quad (12)$$

where x_c is a constant. For the LRI (Abich et al. (2019)), $x_c = 1 \times 10^{-15}$. The rpsd of the LRI range acceleration noise is

$$\sqrt{S_{\text{LRI}}(f)} = (2\pi f)^2 \cdot \tilde{x}_{\text{LRI}}(f). \quad (13)$$

Take for the accelerometer measurement noise rpsd on a single satellite of GRACE and GRACE-FO (Touboul et al. (1999))

$$\sqrt{S_{\text{ACC}_1}(f)} = \tilde{a}_0 \sqrt{1 + \left(\frac{f_k}{f}\right)^2}. \quad (14)$$

Estimates of \tilde{a}_0 and f_k range from $3 \times 10^{-11} \text{ m/s}^2/\sqrt{\text{Hz}}$ and 10 mHz, respectively (Hauk and Wiese (2020)) to $1 \times 10^{-10} \text{ m/s}^2/\sqrt{\text{Hz}}$ and 5 mHz, respectively (Christophe et al. (2010), Conklin and Nguyen (2017)). We take as a compromise $\tilde{a}_0 = 7 \times 10^{-11} \text{ m/s}^2/\sqrt{\text{Hz}}$ and $f_k = 5 \text{ mHz}$. Assuming that the acceleration measurements on the two satellites are uncorrelated, the total accelerometer noise is double: $S_{\text{ACC}} = 2S_{\text{ACC}_1}$.

Improved accelerometers in future missions (Christophe et al. (2010), Conklin and Nguyen (2017)) may have $\tilde{a}_0 = 7 \times 10^{-13} \text{ m/s}^2/\sqrt{\text{Hz}}$.

The total instrument noise power spectral density is

$$S_a = S_{\text{ACC}} + S_{\text{LRI}}. \quad (15)$$

Figure 4 shows $\sqrt{S_a}$ for different ranging instrument and accelerometer noise spectra. The MWI ranging noise is approximated by white displacement noise, $\tilde{x}_{\text{MWI}} = 6 \times 10^{-7} \text{ m}/\sqrt{\text{Hz}}$. This estimate is based on comparing MWI range measurements to simultaneous LRI range measurements. To guide the eye to the frequencies that have the largest signal, $|a_R(f)|$ for a 1 Gt point source from Figure 3 is overlaid as the solid black line. The units of $|a_R|$ are m/s.

As in Section 2, define the SNRD for range acceleration

$$W'_a(f) = \frac{|a_R(f)|^2/M^2}{S_a(f)}. \quad (16)$$

$W_a(f) = W'_a M^2$ is shown in Figure 5 for several values of L . The oscillations with nulls at multiples of $1/\tau = v_o/L$ degrade ρ for L beyond an optimum spacecraft separation.

The optimal signal-to-noise ratio per unit mass is

$$\rho' = \sqrt{4 \int_0^\infty W'_a(f) df}, \quad (17)$$

and the source mass that gives $\rho = 3$ is (cf. Equation 5)

$$M_3 = \frac{3}{\sqrt{4 \int_0^\infty W'_a(f) df}}. \quad (18)$$

From Equations 11 through 16 and Equation 18, the GRACE-FO parameters with the microwave ranging instrument (MWI) and LRI give respectively $M_3 = 1.3 \text{ Gt}, 0.5 \text{ Gt}$.

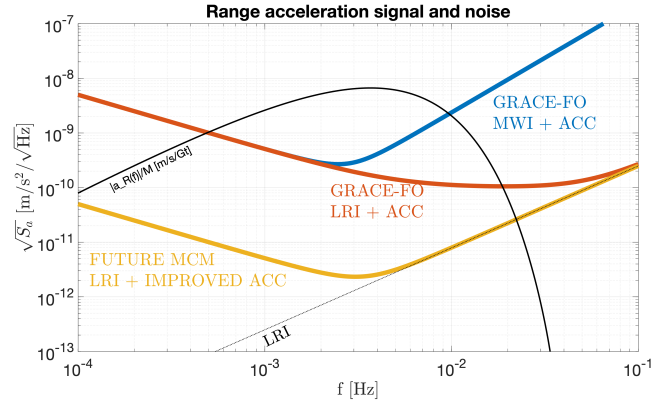


Fig. 4. Total range acceleration noise rpsd $\sqrt{S_a}$ for various assumptions of instrument noise. The ranging noise for the “GRACE-FO MWI+ACC” is the white displacement noise of the microwave measurement on GRACE-FO, equal to $6 \times 10^{-7} \text{ m}/\sqrt{\text{Hz}}$. The other two noise curves assume the ranging noise of the LRI, Equation 12, shown as a dotted line. Two levels of $\tilde{a}_0/[\text{m/s}^2/\sqrt{\text{Hz}}]$ are assumed: 7×10^{-11} for the GRACE-FO curves, and 7×10^{-13} for a future mission such as Mass Change Mission (MCM). The solid black line is the signal spectrum $a_R(f)$ from a 1 Gt point mass, for $h = 500 \text{ km}$ and $L = 200 \text{ km}$, units m/s. The values of M_3 for the three respective configurations are (Section 3.3) 1.3 Gt and 0.5 Gt and 7 Mt.

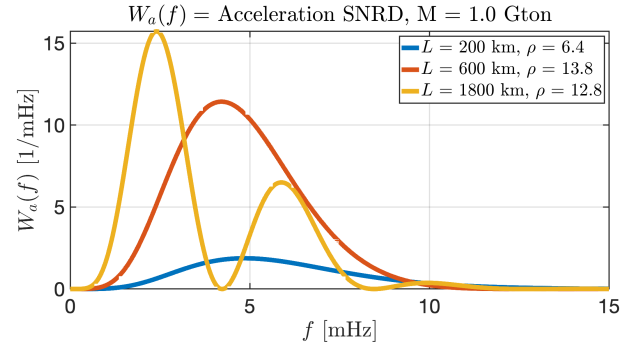


Fig. 5. Signal-to-noise ratio integrand of Equation 16, $W_a(f)$ for the “GRACE-FO LRI + ACC” noise of Figure 4, signal from orbital $h = 500 \text{ km}$ and source mass $M = 1 \text{ Gt}$ and three different values of spacecraft separation L . The integrated signal-to-noise ratios ρ from Equation 17 are indicated in the legend.

The corresponding detectable peak accelerations, $\kappa_R M_3$, are $0.13 \text{ nm/s}^2, 0.047 \text{ nm/s}^2$.

Another assessment of mass sensitivity for SST laser ranging is inferred from Colombo and Chao (1992), who proposed a laser ranging mission that, with $(h, L) = (600, 500) \text{ km}$ was found by simulation to have sensitivity to weekly changes of 1 mm water height over a square region 400 km across, or mass sensitivity of 160 Mt. In comparison, we find for the LRI on GRACE-FO at the same (h, L) , $M_3 = 400 \text{ Mt}$. The two measurements have different assumed instrument sensitivity and averaging times (week-to-week vs. single-pass).

Figure 6 shows the mass sensitivity M_3 as a function of h and L for the LRI ranging instrument with two different levels of accelerometer sensitivity: $\tilde{a}_0 = 7 \times 10^{-11}$ and $7 \times 10^{-13} \text{ m/s}^2/\sqrt{\text{Hz}}$. The lower row of Figure 6 shows the optimum L for a given h and the resulting M_3 . The optimum L for the LRI on GRACE-FO, operating at $h = 500 \text{ km}$, is

$L = 900$ km, which would give $M_3 = 200$ Mt. That reflects a potential factor of 2.5 improvement over $M_3 = 500$ Mt for the nominal satellite separation of $L = 200$ km. A future mission with the improved \tilde{a}_0 , $h = 500$ km, and optimal satellite separation $L = 900$ km has $M_3 = 7$ Mt.

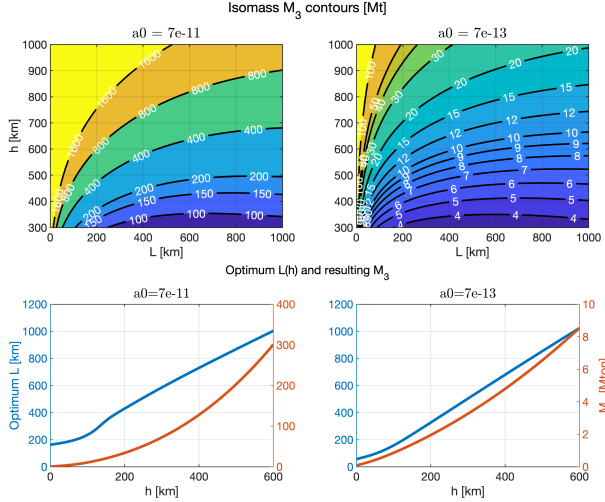


Fig. 6. Mass sensitivity of the LRI measurement on GRACE-FO *left*, and of a future GRACE-like mission *right*. Upper row shows isomass M_3 contours, in Mt, from Equation 18. Equation 12 specifies the ranging noise, and accelerometer noise is given by Equation 14 with $\tilde{a}_0 = (7 \times 10^{-11}, 7 \times 10^{-13})$ m/s²/√Hz, with fixed $f_k = 5$ mHz. Lower row shows the optimum L as a function of h , (blue, left axis) and the resulting sensitivity M_3 (red, right axis).

3.4. Optimal filter

The filter that gives maximum signal-to-noise ratio is (Wainstein and Zubakov (1970), Chapter 3)

$$G(f) = \frac{a_R^*(f)}{S_a(f)}, \quad (19)$$

with * denoting complex conjugation. The filter's input is the measured range acceleration. $G(f)$ is an example of a filter for extracting a signal of known waveform, in this case the range acceleration resulting from flying over a point mass. Dropping the multiplicative constants, the filter magnitude is

$$|G(f)| = \frac{\left| f K_0 \left(\frac{2\pi f}{f_h} \right) \sin \left(\frac{2\pi f}{f_L} \right) \right|}{S_a(f)}. \quad (20)$$

Normalized $|G(f)|$ for the MWI and LRI on GRACE-FO are shown in Figure 7.

Ghobadi-Far et al. (2018) analyzed the GRACE-FO MWI signal in terms of the line-of-sight gravity difference, and applied the same analysis method to the GRACE-FO LRI signal in Ghobadi-Far et al. (2020). In their analysis of MWI data, Ghobadi-Far et al. (2018) defined the gravimetric quantity $\delta g_{12}^{\text{LOS}}$, or line-of-sight (LOS) gravity difference, which differs from the range acceleration residual $\delta \ddot{p}$ by Δ_0 , the residual centrifugal acceleration:

$$\delta g_{12}^{\text{LOS}} = \delta \ddot{p} + \Delta_0. \quad (21)$$

Residuals are relative to a reference field. The admittance $Z(f)$ is defined as the ratio of power spectra,

$$Z(f) = \frac{S_{\delta \ddot{p}, \delta g_{12}^{\text{LOS}}}(f)}{S_{\delta \ddot{p}, \delta \ddot{p}}(f)}, \quad (22)$$

where $S_{\delta \ddot{p}, \delta \ddot{p}}(f)$ is the power spectrum of the MWI range acceleration measurement and $S_{\delta \ddot{p}, \delta g_{12}^{\text{LOS}}}(f)$ is the cross-power spectrum between the range acceleration and the LOS gravity difference. Keeping the shorthand notation $p(f) = \mathcal{F}[p(t)]$, $Z(f)$ is a filter that transforms residual range acceleration $\delta \ddot{p}(f) = a_R(f)$ to $\delta g_{12}^{\text{LOS}}(f)$, an estimate of $\delta g_{12}^{\text{LOS}}(f)$:

$$\delta g_{12}^{\text{LOS}}(f) = Z(f) \delta \ddot{p}(f). \quad (23)$$

$Z(f)$, normalized to have a maximum value of 1, is shown as the dashed trace in Figure 7. $Z(f)$ is the optimal filter to apply to MWI range acceleration, based on the measurement data that includes signal from the gravity field. It applies to extracting the best SNR from a residual regional or global field and does not explicitly depend on instrument noise spectra.

In contrast, $G(f)$ is fine-tuned to the problem of detecting the specific waveform of a point mass, in the presence of known measurement noise. Since a point mass generates a field with the highest possible frequency content, the $G(f)$ passband starts higher in frequency than $Z(f)$. The LRI $G(f)$ passband is higher than for the MWI because the LRI measurement has reduced noise at high frequency.

A practical use for the $G(f)$ filter is searching for unknown point-like features, such as underground water storage of 100 km spatial extent. The filter would be applied to range acceleration measurements after subtracting the effect of the known field, including time-varying gravity, and non-gravitational accelerations.

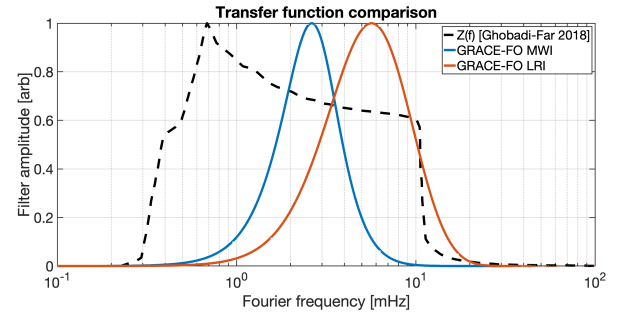


Fig. 7. Transfer functions for range acceleration data. The blue trace that peaks at 2.6 mHz is $|G(f)|$ for the MWI on GRACE-FO, and the red trace that peaks at 5.7 mHz is for the LRI on GRACE-FO. $Z(f)$ is the admittance filter from Ghobadi-Far et al. (2018) Figure 2(b), and applies to the MWI on GRACE-FO. All curves are normalized to give maximum value of 1.

4. Conclusion

We derived the optimum sensitivity of orbiting gravimetric satellites to a point source, that is a single mascon. The signal-to-noise ratio is found as a function of instrument noise and orbital parameters. The signal is converted to frequency space

by the Fourier transform, and the signal-to-noise ratio is derived from optimal filtering a signal of known waveform. This analysis differs from the conventional approach of spherical harmonic expansion to characterize the field from an arbitrary mass distribution. Such an expansion requires a very large harmonic order to accurately approximate the field from a point source, as shown in Appendix A.

The frequency response of an orbiting gradiometer to a point mass directly under the flight track is approximated by Equation 2 that depends only on the orbital altitude and the magnitude of the point mass. Likewise, for an SST-based measurement of the gravitational field, the range acceleration is approximated by Equation 11 that includes dependency on the average satellite separation. Applying Wiener optimal filter theory, these responses and the noise spectra of the ranging measurement and of accelerometer-based measurement of non-gravitational forces give ρ , the maximum achievable signal-to-noise ratio. The resolvable mass M_3 is defined as the magnitude of the point mass that gives $\rho = 3$. M_3 is the ultimate mass sensitivity, and realistic non-point mass distributions that are not directly under the flight track will give larger M_3 in practice. Nonetheless, M_3 provides a figure of merit for comparing future missions with different orbits and instrument sensitivities to guide the design of such missions. For SST measurements M_3 has a minimum value at a calculable satellite separation L , giving the optimum separation for discovering point-like (meaning less than approximately 300 km) features such as subsurface water storage. Equation 20 specifies the optimal filter for such a search. As a caveat, the M_3 metric and its L optimization does not apply to large-scale gravimetry, such as required by oceanography.

Acknowledgments

The author thanks Kirk McKenzie, Gabriel Ramirez, Pep Sanjuan and David Wiese for useful discussions, and Christopher McCullough for key insights. The contributions of four anonymous reviewers, who suggested improvements that are incorporated in this manuscript, is gratefully acknowledged. This research was carried out at the Jet Propulsion Laboratory, California Institute of Technology, under a contract with the National Aeronautics and Space Administration. ©2020 California Institute of Technology. Government sponsorship acknowledged.

Appendix A. Multipole expansion and the Wahr equation for surface density

The gravitational potential is conventionally expressed as the multipole expansion (Kaula (1966), Kaula (2013), Chao and Gross (1987))

$$U(r, \theta, \phi) = \frac{GM_e}{a} \sum_{n=0}^{\infty} \sum_{m=0}^n \left(\frac{a}{r}\right)^{n+1} \bar{P}_{nm}(\cos \theta) \times (\bar{C}_{nm} \cos m\phi + \bar{S}_{nm} \sin m\phi). \quad (\text{A.1})$$

As illustrated in Figure A.8 (r, θ, ϕ) = (distance from the center of the Earth, co-latitude, longitude), (a, M_e) = (Earth radius,

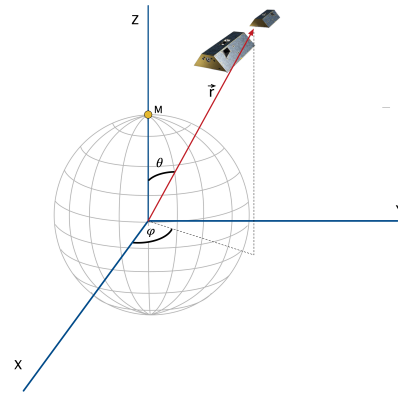


Fig. A.8. Coordinate system for the spherical harmonic expansion of geopotential, Kaula (2013). The satellite constellation position, defined as the center of mass for a gradiometer or (illustrated) the center of the line of sight between two SST satellites relative to the center of the Earth, is $\vec{r}(r, \theta, \phi)$, where r is the distance from the center of the Earth, θ is the co-latitude, and ϕ is the longitude.

Earth mass), and \bar{P}_{nm} is the fully-normalized associated Legendre function. The field is entirely specified by the Stokes coefficients ($\bar{C}_{nm}, \bar{S}_{nm}$).

For a known mass distribution $dM = \rho(r', \theta', \phi')dV'$ with primes designating the source mass coordinates, ($\bar{C}_{nm}, \bar{S}_{nm}$) are evaluated as the volume integral Bettadpur (2018)

$$\left[\begin{array}{c} \bar{C}_{nm} \\ \bar{S}_{nm} \end{array} \right] = \frac{1}{(2n+1)M_e} \int_{V'} dM \left(\frac{r'}{a}\right)^n \bar{P}_{nm}(\lambda') \left[\begin{array}{c} \cos m\phi' \\ \sin m\phi' \end{array} \right], \quad (\text{A.2})$$

where $\lambda' = \cos \theta'$. For a point mass at $r' = a$

$$\left[\begin{array}{c} \bar{C}_{nm} \\ \bar{S}_{nm} \end{array} \right] = \frac{M}{(2n+1)M_e} \bar{P}_{nm}(\lambda') \left[\begin{array}{c} \cos m\phi' \\ \sin m\phi' \end{array} \right]. \quad (\text{A.3})$$

A single point mass can be placed at the north pole, $(\theta', \phi') = (0, 0)$ without loss of generality. Then

$$\left[\begin{array}{c} \bar{C}_{nm} \\ \bar{S}_{nm} \end{array} \right] = \frac{M}{(2n+1)M_e} \bar{P}_{nm}(1) \left[\begin{array}{c} 1 \\ 0 \end{array} \right]. \quad (\text{A.4})$$

The relationship between the fully normalized Legendre function \bar{P}_{nm} and the associated Legendre function P_{nm} is

$$\bar{P}_{nm} = \sqrt{\frac{(2 - \delta_{m0})(2n+1)(n-m)!}{(n+m)!}} P_{nm}, \quad (\text{A.5})$$

where δ_{mn} is the Kronecker delta. Since $P_{nm}(1) = \delta_{m0}$, $\bar{P}_{nm}(1) = \delta_{m0} \sqrt{2n+1}$. For a point mass at the pole Equation A.3 reduces to

$$\left[\begin{array}{c} \bar{C}_{nm} \\ \bar{S}_{nm} \end{array} \right] = \frac{M}{M_e} \frac{1}{\sqrt{2n+1}} \left[\begin{array}{c} \delta_{m0} \\ 0 \end{array} \right]. \quad (\text{A.6})$$

The potential from Equations A.1 and A.6 is independent of ϕ and is given by the multipole expansion

$$U(r, \theta) = \frac{GM}{a} \sum_{n=0}^{\infty} \left(\frac{a}{r}\right)^{n+1} P_n(\cos \theta), \quad (\text{A.7})$$

the familiar expansion from electrostatics for the azimuthally symmetric electric field from a point charge (Jackson (2007)) and from gravitational potential theory (Blakely (1996), Section 6.4.2).

The Wahr equation for surface density from $(\bar{C}_{nm}, \bar{S}_{nm})$ (Wahr et al. (1998)) is

$$\sigma(\theta', \phi') = \frac{a\rho_{\text{ave}}}{3} \sum_{n=0}^{\infty} \sum_{m=0}^n \bar{P}_{nm}(\cos \theta') \frac{2n+1}{1+k_n} \times (\bar{C}_{nm} \cos m\phi' + \bar{S}_{nm} \sin m\phi'), \quad (\text{A.8})$$

where $k_n = \text{Love number}$.

To study the error of a finite-degree spherical harmonic approximation to a point mass, consider a spherical cap in the limit of small cap size. The spherical cap is centered at coordinates (θ', ϕ') and its angular radius is α and $\lambda \equiv \cos \alpha$. As computed by Pollack (1973), the Stokes coefficients are

$$\begin{bmatrix} \bar{C}_{nm} \\ \bar{S}_{nm} \end{bmatrix} = -\frac{M}{M_e} \frac{P_{n+1} - P_{n-1}}{(2n+1)^2(1-\lambda)} \bar{P}_{nm}(\cos \theta') \begin{bmatrix} \cos m\phi' \\ \sin m\phi' \end{bmatrix}, \quad (\text{A.9})$$

where we use the shorthand $P_j(\lambda) = P_j$. For a spherical cap at the north pole,

$$\begin{bmatrix} \bar{C}_{nm} \\ \bar{S}_{nm} \end{bmatrix} = -\frac{M}{M_e} \frac{P_{n+1} - P_{n-1}}{(2n+1)^{3/2}(1-\lambda)} \begin{bmatrix} \delta_{m0} \\ 0 \end{bmatrix}. \quad (\text{A.10})$$

The spherical cap reduces to a point mass in the limit of $\alpha = 0$, or $\lambda = 1$; substituting

$\lim_{\lambda \rightarrow 1} [P_{n+1} - P_{n-1}] = (\lambda - 1)(2n + 1) = \text{into Equation A.10}$ gives Equation A.6.

By comparing expressions similar to Equation A.1 and Equation A.8, Dickey et al. (1997) identifies

$$\hat{C}_{nm} + \hat{S}_{nm} = \frac{\rho_{\text{ave}}}{3\rho_w} \frac{2n+1}{1+k_n} (\bar{C}_{nm} + \bar{S}_{nm}) \quad (\text{A.11})$$

where ρ_w is the density of water as the transformation to convert geoid expansion coefficients $(\bar{C}_{nm}, \bar{S}_{nm})$ to mass expansion coefficients $(\hat{C}_{nm}, \hat{S}_{nm})$, p. 101 their Equation (B5).

At the pole, from Equation A.8, dropping the $n = 0$ term that represents the total potential of the Earth, and neglecting the Earth's elasticity by setting $k_n = 0$,

$$\sigma = \frac{a\rho_{\text{ave}}}{3} \sum_{n=1}^{\infty} \bar{P}_{nm}(1)(2n+1)\bar{C}_{nm}. \quad (\text{A.12})$$

From Equation A.10,

$$\begin{aligned} \sigma &= -\frac{M}{M_e} \frac{a}{1-\lambda} \frac{\rho_{\text{ave}}}{3} \\ &\times \sum_{n=1}^{\infty} \bar{P}_{nm}(1) \frac{2n+1}{(2n+1)^{3/2}} (P_{n+1} - P_{n-1}) \\ &= -\frac{M}{M_e} \frac{a}{1-\lambda} \frac{\rho_{\text{ave}}}{3} \sum_{n=1}^{\infty} P_{n+1} - P_{n-1} \\ &= \frac{M}{M_e} \frac{a\rho_{\text{ave}}}{3} T_{\infty}. \end{aligned} \quad (\text{A.13})$$

The quantity T_{∞} is the $N = \infty$ limit of the truncated sum, defined as

$$\begin{aligned} T_N(\lambda) &= \frac{1}{1-\lambda} \sum_{n=1}^N P_{n-1} - P_{n+1} \\ &= \frac{1}{1-\lambda} (P_0 + P_1 - (P_N + P_{N+1})) \\ &= \frac{1+\lambda - (P_N + P_{N+1})}{1-\lambda}. \end{aligned} \quad (\text{A.14})$$

For a small spherical cap, $\alpha \ll 1$ (and $\lambda = \cos \alpha$ slightly < 1), the cap area is $A = \pi(\alpha a)^2$. Using $\sigma = M/A$ and $\rho_{\text{ave}} = 3M_e/(4\pi a^3)$, Equation A.13 is equivalent to

$$\frac{\alpha^2 T_{\infty}(\cos \alpha)}{4} - 1 = 0. \quad (\text{A.15})$$

The fractional error in σ due to truncation of the summation Equation A.13 at order N is

$$\epsilon_N = \frac{\alpha^2 T_N(\cos \alpha)}{4} - 1 \approx -P_N(\cos \alpha). \quad (\text{A.16})$$

See Figure A.9 for ϵ_N with small spherical caps of two different sizes. The slow reduction of $|\epsilon_N|$ with increasing N shows that the unfiltered spherical harmonic expansion is ill-suited to characterize the field from a point-like source. The truncation error is often reduced by applying a spectral localizing filter (Panet et al. (2013), Appendix 2); see also Wahr et al. (1998), Swenson and Wahr (2002), Seo et al. (2005), and Werth et al. (2009).

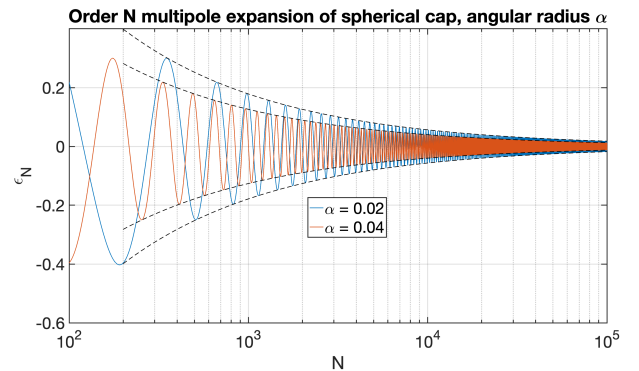


Fig. A.9. Truncation error, Equation A.16, in representing the field from a mass of small spatial extent by spherical harmonic expansion of order N . The dashed lines follow the large N asymptote envelope, $\pm P_N(\cos \alpha) \sim \pm \sqrt{2/(\pi N \sin \alpha)}$.

References

- Abich, K., Abramovici, A., Amparan, B., Baatzsch, A., Bachman Okihiro, B. B., Barr, D. C., Bize, M. P., Bogan, C., Braxmaier, C., Burke, M. J., et al. (2019). In-orbit performance of the GRACE Follow-on laser ranging interferometer. *Physical Review Letters*, 123(3):031101.
- Abramowitz, M. and Stegun, I. A. (1964). *Handbook of Mathematical Functions with Formulas, Graphs, and Mathematical Tables*. Dover, New York, ninth Dover printing, tenth GPO printing edition.
- Bettadpur, S. (2018). *GRACE L-2 Product User Manual*. Center for Space Research, The University of Texas at Austin. GRACE 327-734, CSR-GR-03-01.

- Blakely, Richard J. (1996). *Potential Theory in Gravity and Magnetic Applications*. Cambridge University Press.
- Chao, B. F. and Gross, R. S. (1987). Changes in the Earth's rotation and low-degree gravitational field induced by earthquakes. *Geophysical Journal International*, 91(3):569–596.
- Christophe, B., Marque, J., and Foulon, B. (2010). In-orbit data verification of the accelerometers of the ESA GOCE mission. In *SF2A-2010: Proceedings of the Annual meeting of the French Society of Astronomy and Astrophysics*, volume 1, page 113.
- Colombo, O. and Chao, B. (1992). Global gravitational change from space in 2001. In *IAG Symp.*, 112, 71–74.
- Conklin, J. and Nguyen, A. N. (2017). Drag-free control and drag force recovery of small satellites. In *31st Annual AIAA/USU Conference on Small Satellites*.
- Dickey, J., Bentley, C. R., Bilham, R., Carton, J., Eanes, R., Herring, T. A., Kaula, W., Lagerloef, G., Rojstaczer, S., Smith, W., et al. (1997). Satellite gravity and the geosphere. *National Research Council Report*, 112.
- Drinkwater, M. R., Haagmans, R., Muzi, D., Popescu, A., Floberghagen, R., Kern, M., and Fehringer, M. (2006). The GOCE gravity mission: ESA's first core Earth explorer. In *Proceedings of the 3rd international GOCE user workshop*, pages 6–8.
- Flanagan, E. E. and Hughes, S. A. (1998). Measuring gravitational waves from binary black hole coalescences. i. signal to noise for inspiral, merger, and ringdown. *Phys. Rev. D*, 57:4535–4565.
- Ghobadi-Far, K., Han, S.-C., Weller, S., Loomis, B. D., Luthcke, S. B., Mayer-Gürr, T., and Behzadpour, S. (2018). A transfer function between line-of-sight gravity difference and GRACE intersatellite ranging data and an application to hydrological surface mass variation. *Journal of Geophysical Research: Solid Earth*, 123(10):9186–9201.
- Ghobadi-Far, K., Han, S.-C., McCullough, C. M., Wiese, D. N., Yuan, D., Landerer, F. W., Sauber, J., Watkins, M. M., (2020) GRACE Follow-On Laser Ranging Interferometer Measurements Uniquely Distinguish Short-Wavelength Gravitational Perturbations. *Geophysical Research Letters*, 47(16):e2020GL089445.
- Han, S.-C. (2013). Determination and localized analysis of intersatellite line of sight gravity difference: Results from the GRAIL primary mission. *Journal of Geophysical Research: Planets*, 118(11):2323–2337.
- Hauk, M. and Wiese, D. N., (2020). New Methods for Linking Science Objectives to Remote Sensing Observations: A Concept Study Using Single- and Dual-Pair Satellite Gravimetry Architectures. *Earth and Space Science*, 7(3):e2019EA000922.
- Jackson, J. D. (2007). *Classical electrodynamics*. John Wiley & Sons.
- Kaula, W. M. (1966). Tests and combination of satellite determinations of the gravity field with gravimetry. *Journal of Geophysical Research*, 71(22):5303–5314.
- Kaula, W. M. (2013). *Theory of satellite geodesy: applications of satellites to geodesy*. Courier Corporation.
- Konopliv, A. S., Park, R. S., Yuan, D.-N., Asmar, S. W., Watkins, M. M., Williams, J. G., Fahnestock, E., Kruizinga, G., Paik, M., Strelakov, D., et al. (2013). The JPL lunar gravity field to spherical harmonic degree 660 from the GRAIL primary mission. *Journal of Geophysical Research: Planets*, 118(7):1415–1434.
- Landerer, F., Flechtner, F., Save, H., Webb, F., Bandikova, T., and Bertiger, W., et al. (2020). Extending the global mass change data record: GRACE follow-on instrument and science data performance. *Geophysical Research Letters*, 47(12).
- McCullough, C., Harvey, N., Save, H., Bandikova, T. (2019). Description of Calibrated GRACE-FO Accelerometer Data Products (ACT) *GRACE-FO Level-1 Product Version 04 Manual* JPL D-103863
- Müller, V. (2017). Design considerations for future geodesy missions and for space laser interferometry Ph.D. Thesis, Gottfried Wilhelm Leibniz Universität Hannover, 2017.
- Numata, K., Kemery, A., and Camp, J. (2004). Thermal-noise limit in the frequency stabilization of lasers with rigid cavities. *Physical Review Letters*, 93(25):250602.
- Panet, I., Flury, J., Biancale, R., Gruber, T., Johannessen, J., van den Broeke, M., van Dam, T., Gegout, P., Hughes, C., Ramillien, G., et al. (2013). Earth system mass transport mission (e. motion): a concept for future Earth gravity field measurements from space. *Surveys in Geophysics*, 34(2):141–163.
- Pollack, H. N. (1973). Spherical harmonic representation of the gravitational potential of a point mass, a spherical cap, and a spherical rectangle. *Journal of Geophysical Research*, 78(11):1760–1768.
- Reigber, C., Schwintzer, P., Neumayer, K.-H., Barthelmes, F., König, R., Förste, C., Balmino, G., Biancale, R., Lemoine, J.-M., Loyer, S., et al. (2003). The CHAMP-only Earth gravity field model EIGEN-2. *Advances in Space Research*, 31(8):1883–1888.
- Seo, K.-W., Wilson, C., Chen, J., Famiglietti, J., and Rodell, M. (2005). Filters to estimate water storage variations from GRACE. In *IAG Symp.*, 128, 607–611. Springer.
- Swenson, S. and Wahr, J. (2002). Methods for inferring regional surface-mass anomalies from gravity recovery and climate experiment (GRACE) measurements of time-variable gravity. *Journal of Geophysical Research: Solid Earth*, 107(B9):ETG–3.
- Tapley, B. D. (1997). Evaluation of Flat-Earth Approximation Results for Geopotential Missions. *Journal of Guidance, Control, and Dynamics*, 20(2):246–252.
- Tapley, B. D., Bettadpur, S., Ries, J. C., Thompson, P. F., and Watkins, M. M. (2004). GRACE measurements of mass variability in the Earth system. *Science*, 305(5683):503–505.
- Touboul, P., Willemenot, E., Foulon, B., and Josselin, V. (1999). Accelerometers for CHAMP, GRACE and GOCE space missions: synergy and evolution. *Boll. Geof. Teor. Appl.*, 40(3-4):321–327.
- Touboul, P., Foulon, B., and Willemenot (1999a). Electrostatic space accelerometers for present and future missions. *Acta Astronautica*, 45(10):605–617.
- Wahr, J., Molenaar, M., and Bryan, F. (1998). Time variability of the Earth's gravity field: Hydrological and oceanic effects and their possible detection using GRACE. *Journal of Geophysical Research: Solid Earth*, 103(B12):30205–30229.
- Wainstein, L. A. and Zubakov, V. (1970). *Extraction of signals from noise*. PrenticeHall, Englewood Cliffs, NJ.
- Watkins, M., Wiese, D. N., Yuan, D.-N., Boening, C., and Landerer, F. W. (2015). Improved methods for observing Earth's time variable mass distribution with GRACE using spherical cap mascons. *Journal of Geophysical Research: Solid Earth*, 120(4):2648–2671.
- Watkins, M., Yuan, D., Kuang, D., Bertiger, W., Kim, M., and Kruizinga, G. (2005). GRACE harmonic and mascon solutions at JPL. *AGU Fall Meeting*, 2005:G22A–04.
- Werth, S., Güntner, A., Schmidt, R., and Kusche, J. (2009). Evaluation of GRACE filter tools from a hydrological perspective. *Geophysical Journal International*, 179(3):1499–1515.
- Wolff, M. (1969). Direct measurements of the Earth's gravitational potential using a satellite pair. *Journal of Geophysical Research*, 74(22):5295–5300.
- Wong, L., Buechler, G., Downs, W., Sjogren, W., Muller, P., and Gottlieb, P. (1971). A surface-layer representation of the lunar gravitational field. *Journal of Geophysical Research*, 76(26):6220–6236.